Available online at www.sciencedirect.com
ScienceDirect
Trans. Nonferrous Met. Soc. China 34(2024) 3949−3962
Transactions of Nonferrous Metals Society of China
www.tnmsc.cn

Effect of Mo substitution of Fe on strength and corrosion resistance of $AlCoCrFe_{1-x}NiMo_x$ high-entropy alloys

Hong-qi SHI[1], Xiao-di JI[2], Dong-hui JIAN[2], Tian-shuo XU[1],
Chen WANG[2], Tao TANG[2,3], Wen-juan LIU[2,3], Zhen-hua CAO[2,3]

1. School of Information Engineering, Suqian University, Suqian 223800, China;
2. College of Materials Science and Engineering, Nanjing Tech University, Nanjing 211816, China;
3. Jiangsu Collaborative Innovation Center for Advanced Inorganic Functional Composites, Nanjing Tech University, Nanjing 211816, China

Received 24 April 2023; accepted 19 December 2023

Abstract: A series of $AlCoCrFe_{1-x}NiMo_x$ high-entropy alloys (HEAs) were fabricated and characterized by XRD, SEM, EDS mapping, compression test, hardness and electrochemistry measurements. The research results indicate that after Mo completely replaces Fe, the compressive strength of the alloys can reach 3181 MPa because the addition of Mo can form σ phase beneficial to the grain refinement, thereby improving the strength of the alloys. However, the addition of Mo has a detrimental effect on corrosion resistance as a result of formation of galvanic cell between the substrate and σ phases. Although most of $AlCoCrFe_{1-x}NiMo_x$ have lower corrosion current densities than pristine alloy, a partial Mo substitution (x=0.25) widens the passivation region of HEAs. The inconsistency of mechanical properties with corrosion resistance is ascribed to different roles of Mo in phase formation and protection of passive film.
Key words: high-entropy alloy; Mo substitution of Fe; compressive strength; corrosion resistance

1 Introduction

High-entropy alloys (HEAs) have drawn extensive attention owing to their outstanding properties such as high strength [1−3], equilibrium of strength and ductility [4−6], high hardness [7,8], and high corrosion resistance [9−11]. HEAs typically contain no less than five metal elements in equal or approximately equal atomic proportions [12−15]. As a classic HEA system, AlCoCrFeNi HEA exhibits excellent comprehensive performances [16−19]. However, AlCoCrFeNi HEAs with insufficient strength and corrosion resistance have been restricted from their practical engineering applications. Recently, various strategies have been adopted to enhance the strength and corrosion resistance of HEAs, including annealing [20,21], alloying [22], and thermal mechanical processing [23].

Among them, alloying is considered to be the most effective method [24], in which the addition of alloying elements optimized the crystal structure, and improved the mechanical properties and corrosion resistance of HEAs. For instance, ZHAO et al [25] investigated the impact of microalloying with titanium on the structure and properties of $Al_{2-x}CoCrFeNiTi_x$. It was found that the BCC1+$B$2 and BCC2+BCC1+$B$2 phases were replaced by BCC2+Laves+BCC1 phases because of alloying. Adding a proper amount of Ti could increase the compressive strength (1919 MPa) and the fracture strain (11.85%) due to the fine grain strengthening and second phase strengthening. Furthermore, the

Corresponding author: Wen-juan LIU, Tel: +86-25-83587270, E-mail: liuwenjuan@njtech.edu.cn
DOI: 10.1016/S1003-6326(24)66650-1

corrosion resistance of $Al_{2-x}CoCrFeNiTi_x$ HEAs can be effectively improved by the replacement of Ti because it widened the passivation interval of HEA. LIU et al [26] explored the influence of Si element on microstructure and the link between structural changes and properties (microhardness and wear behavior) of $AlCoCrFeNiSi_x$ coatings. The grain size was refined and trace $Cr_{23}C_6$ phase formed along the grain boundaries as the Si was added. At the same time, the enhancement of dislocation led to an increase in microhardness. Due to the lubricating effect of SiO_2 and SiO in the oxide film during the wear process, the friction coefficient of the material was reduced and wear resistance was enhanced.

Mo addition is facilitated to strengthen the mechanical performances of HEAs. WEI et al [27] increased the yield strength of $Fe_{40}Mn_{40}Co_{10}Cr_{10}$ high-entropy alloy from 240 to 560 MPa by adding Mo and C, which was mainly due to solid solution strengthening of microelements Mo and C. Meanwhile, C and Mo accelerated the deformation twinning of the alloy which enhanced the working hardening ability. Meanwhile, Mo addition can improve the corrosion sensitivity of HEAs by enhancing the stability of passivation film. CHOU et al [28] disclosed that Mo element inhibited pitting corrosion and expanded passivation interval of $CrCo_{1.5}FeNi_{1.5}Ti_{0.5}Mo_x$ HEAs in 1 mol/L NaCl solution. Although it has been widely researched that Mo element made an important contribution to the improvement of mechanical properties and corrosion resistance of HEAs [29], there is no report on the substitution of Fe by Mo in AlCoCrFeNi HEAs. As known, Fe is easy to corrode and the passive film is not dense. Al, Cr, and Ni are all passive elements. Mo substitution to Fe may improve corrosion resistance of AlCoCrFeNi HEAs.

In the present work, a series of $AlCoCrFe_{1-x}NiMo_x$ (x=0, 0.25, 0.5, 0.75, and 1 at.%) HEAs were designed and fabricated. The effect of Mo substitution to Fe in $AlCoCrFe_{1-x}NiMo_x$ HEAs on microstructure and mechanical properties was systematically investigated by various physical characterizations and compression tests. Later, the relationship between the corrosion performance and the amount of Mo addition was explored in NaCl solution (3.5 wt.%). This work was aimed to provide a route to further improve the mechanical strength and corrosion resistance of AlCoCrFeNi HEA for future engineering applications.

2 Experimental

A series of $AlCoCrFe_{1-x}NiMo_x$ (x=0, 0.25, 0.5, 0.75, and 1 at.%) HEA ingots were prepared by arc melting different granulated metals of greater than 99.9% purity in a copper crucible under a high purity argon atmosphere, and the ingots were named according to different Mo-to-Fe ratios (Fe_1Mo_0, $Fe_{0.75}Mo_{0.25}$, $Fe_{0.5}Mo_{0.5}$, $Fe_{0.25}Mo_{0.75}$, and Fe_0Mo_1). After repeated melting at least 5 times to ensure uniformity, the molten liquid metal was then sucked into a copper mold with a diameter of 6 mm to obtain the cylindrical sample. Cylindrical alloys were cut to the required size for different tests and polished with SiC sandpaper from low to high mesh. Finally, the specimens were rinsed with alcohol and then vacuum-dried.

The structures of HEAs were characterized by an X-ray diffractometer (XRD, ARL X'TRA) using Cu K_α radiation (40 kV, 100 mA) with 2θ from 20° to 80° at a scanning rate of 10 (°)/min. A scanning electron microscope (SEM, FEI Nova NanoSEM 450) equipped with energy dispersive X-ray spectroscopy (EDS) was applied to characterizing the microstructure and the chemical composition. A total of five backscattered electron (BSE) images under different conditions were utilized for averaging.

For analyzing the mechanical properties of alloy samples (d6 mm × 12 mm), compression tests were performed on an electronic universal testing machine (WDW−20) at a constant displacement speed of 1 mm/min and room temperature. Subsequently, the fracture morphology of recovered fracture specimens was observed by SEM.

All electrochemical tests were conducted in 3.5 wt.% NaCl solution by using an electrochemical workstation (CHI 660E) at room temperature. The working electrode (WE) was prepared by polishing alloys with a surface area of 0.29 cm^2. A saturated calomel electrode (SCE) and a Pt plate were respectively adopted as the reference electrode and counter electrode. At first, open circuit potential (OCP) was monitored about 60 min until it became stable. The scanning rate of potentiodynamic polarization tests was set to 1 mV/s and the test range was from −0.6 V (vs SCE) to 0.8 V (vs SCE).

Electrochemical impedance spectrum (EIS) tests were performed at an amplitude of 10 mV with frequencies ranging from 10^5 Hz to 10^{-2} Hz.

3 Results and discussion

3.1 Chemical compositions and microstructures

Figure 1 presents the XRD patterns of $AlCoCrFe_{1-x}NiMo_x$ HEAs. When there is no Mo, the phase composition of AlCoCrFeNi HEA is BCC+*B*2 (ordered BCC phase) phases [30]. The 2θ peak positions of BCC phase are at 44.5° and 64.7°, while that of *B*2 is at 30.1°. The peak of the σ phase is observed between 40° and 50°, while the peak of the *B*2 phase disappears in Mo-containing alloys [31]. This indicates that the phase composition of $AlCoCrFe_{1-x}NiMo_x$ HEAs is transformed from BCC+*B*2 to BCC+σ phases after the Mo element is added. With the increase of the ratio of Mo to Fe, the peak intensity of the σ phase gradually increases relative to that of BCC, demonstrating that the amount of σ phase increases whereas that of the BCC phase decreases. Meanwhile, the peak position of the σ phase deviates from the starting position, indicating that Mo enlarges the lattice distortion energy of the alloys as a result of the larger atomic radius of Mo. The BCC and σ phases in XRD patterns displayed in Fig. 1 are confirmed to be Al−Ni and Mo−Cr phases, respectively [32].

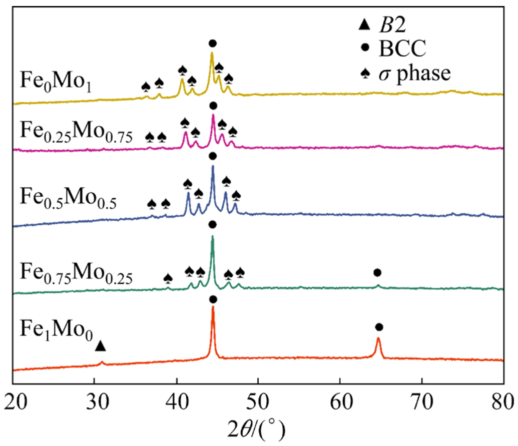

Fig. 1 XRD patterns of $AlCoCrFe_{1-x}NiMo_x$ alloys

The backscattered electron (BSE) images in Fig. 2 show the microstructures for as-cast $AlCoCrFe_{1-x}NiMo_x$ HEAs. Figure 2(a) indicates that the microstructure of Fe_1Mo_0 alloy is relatively uniform without obvious segregation. The inner grain of Fe_1Mo_0 alloy is composed of two phases alternating interdendritic and dendrite, which is a nanoscale amplitude-modulated decomposition structure, where the interdendritic region is *B*2 phase and the dendrite region is BCC phase. Both the Fe_1Mo_0 and $Fe_{0.75}Mo_{0.25}$ alloys display an equiaxed dendritic grain structure. But segregation is more obvious in $Fe_{0.75}Mo_{0.25}$ alloy because $Fe_{0.75}Mo_{0.25}$ alloy has a larger solidification range and a larger component supercooling than Fe_1Mo_0 alloy. In the enlarged image of Fig. 2(b), the interdimeric region is alternated between the BCC phase and σ phase. Due to the high melting point of Mo element, the addition of Mo raises the overall melting point of the alloy, and the undercooling degree increases in the solidification process, which promotes the formation of dendrite. Figures 2(c−e) show the backscattering images of $Fe_{0.5}Mo_{0.5}$, $Fe_{0.25}Mo_{0.75}$, and Fe_0Mo_1 alloys, respectively. These three samples are all non-equiaxed dendritic structures. In $Fe_{0.5}Mo_{0.5}$ alloy, the σ phase and BCC phase are in lamellar distribution in the interdendritic region, while in $Fe_{0.75}Mo_{0.25}$ and Fe_0Mo_1 alloys, the element segregation is more obvious. Scholars commonly use the concept of partition ratio to regulate the γ/γ' volume fraction in high-temperature nickel-based alloys as the means of improving alloy properties [33]. That is to say, if the σ phase contains a large amount of specific element, then this element can be considered as a forming or stabilizing element of the σ phase, thus increasing the volume fraction σ phase. The number of dendrite integrals in the alloys was measured, and it was found that the content of dendrite gradually decreased with the increase of Mo content (Fig. 2(f)). The volume fraction of σ phase in the $Fe_{0.75}Mo_{0.25}$, $Fe_{0.5}Mo_{0.5}$, $Fe_{0.25}Mo_{0.75}$, and Fe_0Mo_1 alloys are 25%, 43%, 49%, and 52%, respectively. According to Table 1, it is not difficult to find that Mo is mainly a solid solution in the σ phase. Mo is a σ forming element in the $AlCoCrFe_{1-x}NiMo_x$ HEAs. However, the dendrite shape becomes finer and more uniform, which will be beneficial to the mechanical properties of the HEAs.

Figure 3 exhibits the EDS mapping images of the as-cast $AlCoCrFe_{1-x}NiMo_x$ HEAs. In Mo-free alloy, all elements are uniformly distributed, which is consistent with XRD and BSE results. Segregation begins to occur in the alloys after the addition of Mo. The dendrite phase is rich in Al and

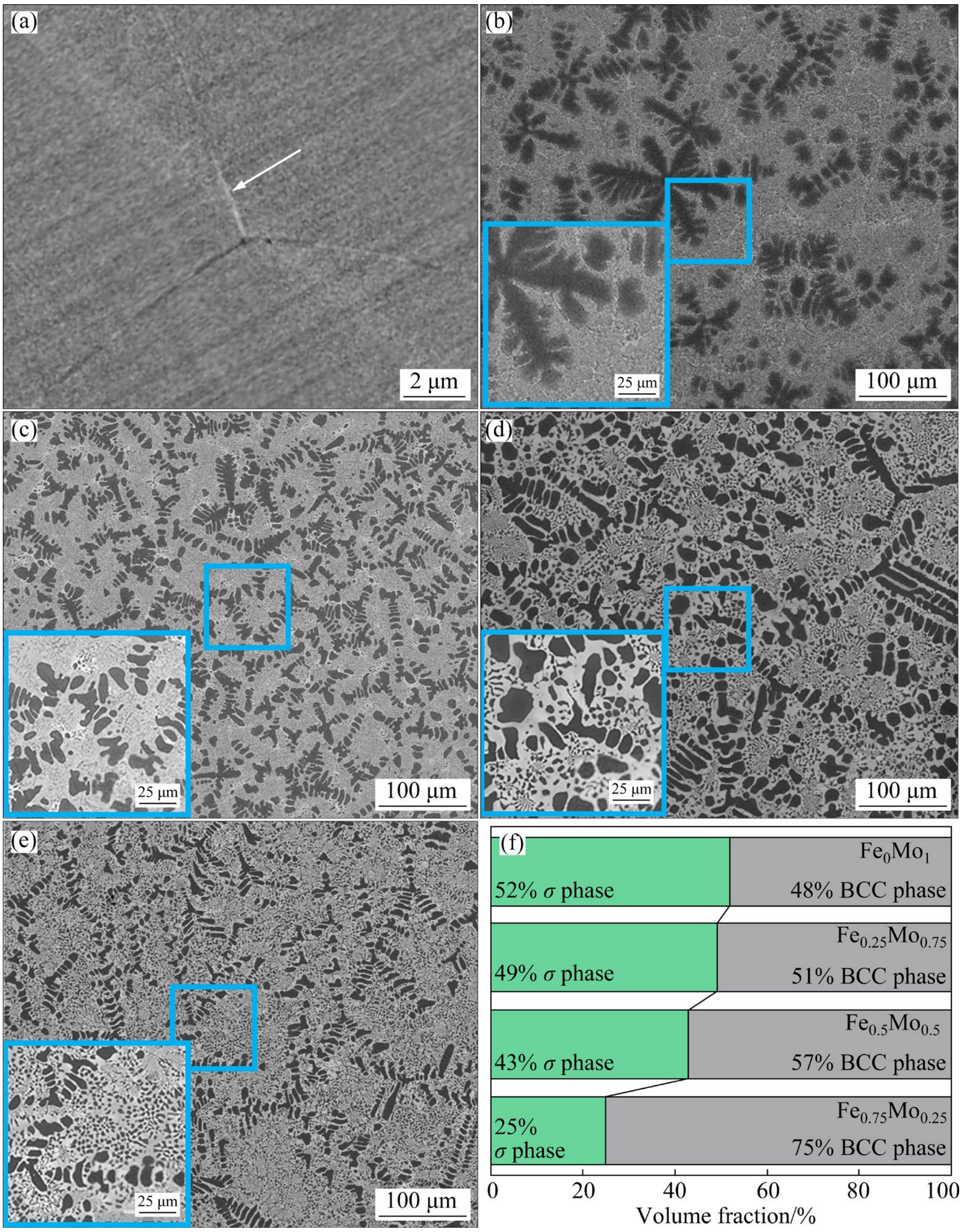

Fig. 2 BSE images of AlCoCrFe$_{1-x}$NiMo$_x$ HEAs: (a) Fe$_1$Mo$_0$; (b) Fe$_{0.75}$Mo$_{0.25}$; (c) Fe$_{0.5}$Mo$_{0.5}$; (d) Fe$_{0.25}$Mo$_{0.75}$; (e) Fe$_0$Mo$_1$; (f) Volume fractions of σ phase in Fe$_{0.75}$Mo$_{0.25}$, Fe$_{0.5}$Mo$_{0.5}$, Fe$_{0.25}$Mo$_{0.75}$, and Fe$_0$Mo$_1$ alloys

Table 1 Mixing enthalpy values of alloy elements [31]

Element	Mixing enthalpy/(kJ·mol^{-1})					
	Al	Co	Cr	Fe	Ni	Mo
Al	–	−19	−10	−11	−22	−5
Co	−19	–	−4	−1	0	−5
Cr	−10	−4	–	−1	−7	0
Fe	−11	−1	−1	–	−2	−2
Ni	−22	0	−7	−2	–	−7
Mo	−5	−5	0	−2	−7	–

Ni, attributing to large negative mixing enthalpy of Al and Ni (Table 1), while Mo and Cr are enriched in the interdendritic phase. However, Fe and Co are uniformly distributed in all samples. The chemical composition of different microstructures for all AlCoCrFe$_{1-x}$NiMo$_x$ HEAs is listed in Table 2. As indicated, the contents of Al and Ni in the dendrite phase are much higher than those in the inter-dendritic phase, while Mo and Cr are much less in the dendrite phase. Taking into account the XRD and BSE analyses, it can be determined that the

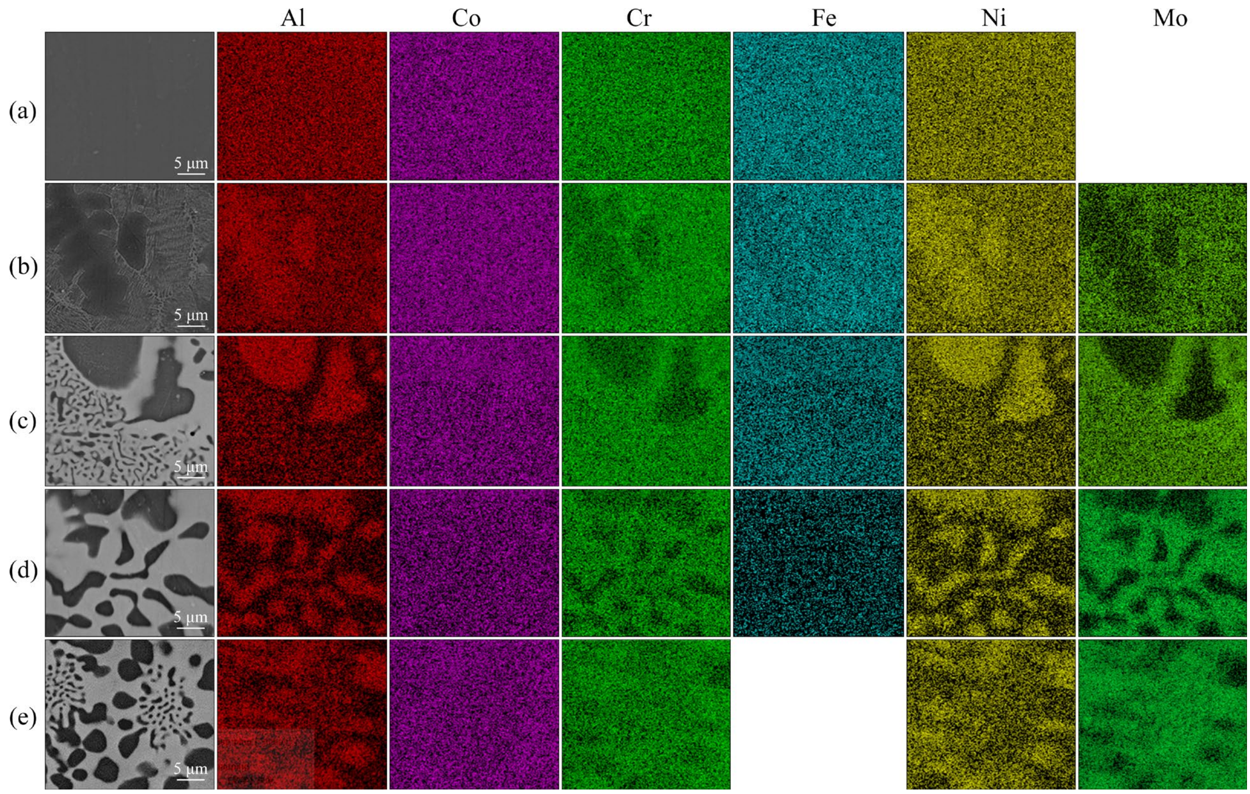

Fig. 3 EDS mapping images of AlCoCrFe$_{1-x}$NiMo$_x$ HEAs: (a) Fe$_1$Mo$_0$; (b) Fe$_{0.75}$Mo$_{0.25}$; (c) Fe$_{0.5}$Mo$_{0.5}$; (d) Fe$_{0.25}$Mo$_{0.75}$; (e) Fe$_0$Mo$_1$

Table 2 Chemical compositions of as-cast AlCoCrFe$_{1-x}$NiMo$_x$ HEAs

Alloy	Region	Content/at.%					
		Al	Cr	Fe	Co	Ni	Mo
Fe$_1$Mo$_0$	Nominal	20.00	20.00	20.00	20.00	20.00	−
	Dendrite	19.89	20.87	20.83	19.41	19.00	−
	Interdendritic	20.81	19.71	19.65	19.98	19.85	−
	Grain boundary	9.05	29.23	25.46	28.22	8.04	−
Fe$_{0.75}$Mo$_{0.25}$	Nominal	20.00	20.00	15.00	20.00	20.00	5.00
	Dendrite	28.09	14.40	12.20	19.49	23.14	2.68
	Interdendritic	16.77	25.82	17.16	18.95	14.27	7.02
Fe$_{0.5}$Mo$_{0.5}$	Nominal	20.00	20.00	10.00	20.00	20.00	10.00
	Dendrite	34.82	10.38	6.56	18.73	26.33	3.19
	Interdendritic	15.31	26.56	11.70	18.90	11.94	15.60
Fe$_{0.25}$Mo$_{0.75}$	Nominal	20.00	20.00	5.00	20.00	20.00	15.00
	Dendrite	30.59	12.03	4.06	20.52	26.78	6.01
	Interdendritic	12.47	27.31	6.63	20.31	11.03	22.24
Fe$_0$Mo$_1$	Nominal	20.00	20.00	−	20.00	20.00	20.00
	Dendrite	27.29	14.52	−	21.50	25.19	11.50
	Interdendritic	8.00	31.50	−	22.99	9.83	27.67

dendrite phase is Al−Ni-rich BCC phase, while the interdendritic phase is the Mo−Cr-rich σ phase. In AlCoCrFeNi HEAs, the Al−Ni-rich BCC phase is at grain boundary. This structure has also been observed in other HEAs [34,35]. It is notable that the composition of the BCC phase has little difference, and the Mo content in the σ phase increases gradually at this state, and is much higher than the theoretical Mo content in the alloy. This indicates that the addition of Mo can promote the segregation of Al and Ni elements to form dendrite, but has a slight effect on the composition of dendrite. Moreover, Mo is solid-dissolved in the σ phase.

In the solidification process, the BCC phase rich in AlNi was formed preferentially, in which Fe and Co elements were also solid-dissolved, and MoCr enriched continuously in the liquid phase. With the solidification process, σ phase rich in MoCr was formed. With the increase of Mo content, the lattice distortion energy in the alloy increased continuously. To reduce the influence of lattice distortion energy, Al and Ni elements were repulsed more intensively, so that the boundary between the σ phase and BCC phase became more obvious. At the same time, the volume fraction of the σ phase increased with the addition of Mo element, and even became the matrix phase in the AlCoCrNiMo alloys, while the amount of BCC phase gradually decreased. It was difficult to form large volume precipitate phases in the solidification process. Therefore, the shape of the BCC phase became finer and the distribution was more uniform.

3.2 Mechanical properties

To further explore the influence of Mo addition on mechanical properties of the alloys, Fig. 4 presents the microhardness of the as-cast AlCoCrFe$_{1-x}$NiMo$_x$ HEAs. The microhardness for Fe$_1$Mo$_0$, Fe$_{0.75}$Mo$_{0.25}$, Fe$_{0.5}$Mo$_{0.5}$, Fe$_{0.25}$Mo$_{0.75}$, and Fe$_0$Mo$_1$ alloys is HV 579, HV 734, HV 909, HV 968, and HV 1111, respectively. The hardness changing trend of the alloys is consistent with molar ratio changes of Mo-to-Fe. The rise of microhardness with the increase of Mo content is attributed to incoherent second phase strengthening effect of the hard and brittle σ phase. Meanwhile, the dissolution of Mo enhances lattice distortion energy and residual stress of alloys, thus resulting in the increased hardness.

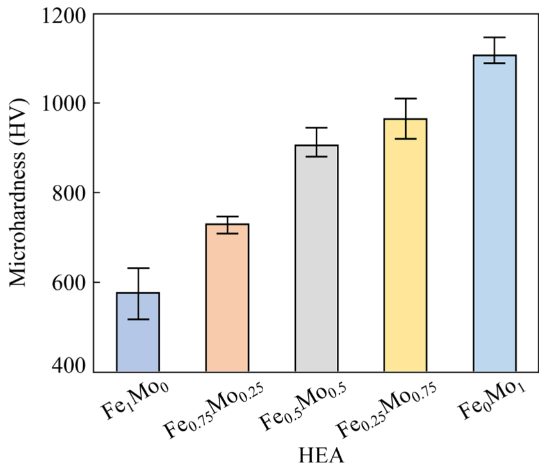

Fig. 4 Microhardness of as-cast AlCoCrFe$_{1-x}$NiMo$_x$ HEAs

Figure 5(a) shows compressive stress−strain curves of AlCoCrFe$_{1-x}$NiMo$_x$ HEAs and Table 3 lists partial important parameters including compressive yield strength (σ_y), compressive fracture strength (σ_{max}), and fracture strain (ε_f). The σ_{max} and ε_f of Fe$_1$Mo$_0$ alloy are 2240 MPa and 16.82%, respectively. When the Mo content is 0.75 at.%, the σ_{max} reaches 2900 MPa, and the compressive strain decreases to 6.52%. The compressive fracture strength of AlCoCrFe$_{1-x}$NiMo$_x$ HEAs reaches the maximum of 3181 MPa when Mo addition is 1 at.%, but the corresponding ductility reduces to 0. The variation trend of compression strength is consistent with that of hardness, while the ductility of the alloy decreases gradually until it disappears. The improvement in compression strength is due to the incoherent second phase strengthening and solution strengthening. Interestingly, after a period of uniform deformation, the inflection points of Fe$_1$Mo$_0$ and Fe$_{0.75}$Mo$_{0.25}$ alloys appear in the stress−strain curves, while the inflection points of Fe$_{0.5}$Mo$_{0.5}$, Fe$_{0.25}$Mo$_{0.75}$, and Fe$_0$Mo$_1$ alloys gradually become inconspicuous until they completely disappear, which is consistent with the previous results [36]. The main reason for the decline in ductility is the formation of the σ phase which is hard and brittle. During the compression process, the hard σ phase is barely deformed and hinders the deformation of the BCC phase, therefore improving the compression strength. Because of a large difference in atomic radius between Mo and other elements, the lattice distortion energy in the σ phase gradually increases

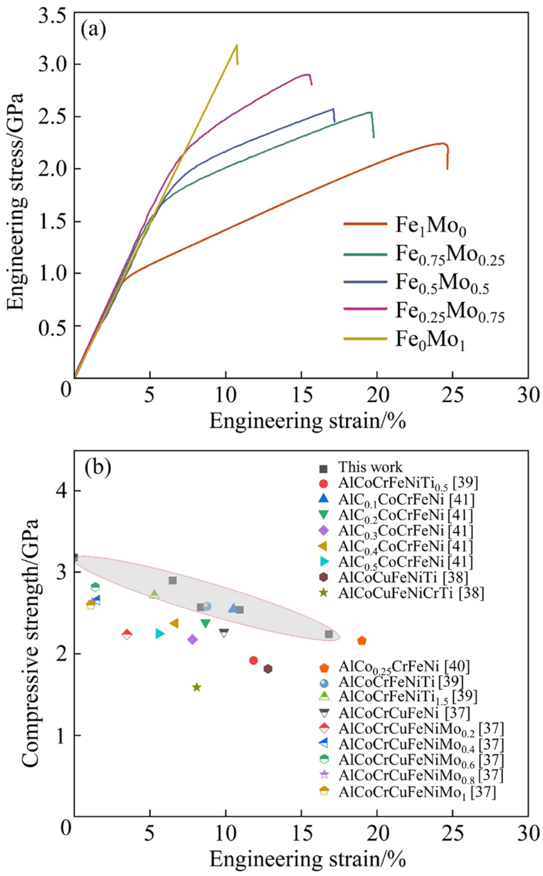

Fig. 5 Mechanical properties of $AlCoCrFe_{1-x}NiMo_x$ HEAs: (a) Mean compressive stress−strain curves of $AlCoCrFe_{1-x}NiMo_x$ HEAs; (b) Mechanical properties for different HEAs [37−41]

Table 3 Compressive properties of $AlCoCrFe_{1-x}NiMo_x$ HEAs

HEA	σ_y/MPa	σ_{max}/MPa	ε_f/%
Fe_1Mo_0	935	2240	16.82
$Fe_{0.75}Mo_{0.25}$	1744	2538	10.95
$Fe_{0.5}Mo_{0.5}$	1804	2573	8.37
$Fe_{0.25}Mo_{0.75}$	2153	2900	6.52
Fe_0Mo_1	−	3181	0

with the increase of Mo element. That is to say, the dislocation slip becomes more difficult, which makes the deformation of the σ phase more difficult and thus improves the strength of the alloy. Meanwhile, because the deformation degree of the two phases is inconsistent, cracks are easier to occur between the two phases. Although the content of the σ phase does not much change, residual internal stress increases with the strengthening of the Mo solution, which leads to a sharp deterioration in ductility. The compression strength of other HEAs [37−41] are compared with our work (shown in Fig. 5(b)), and it is obvious that the $Fe_{0.25}Mo_{0.75}$ alloy exhibits excellent mechanical properties.

Figure 6 displays the fracture surface images of $AlCoCrFe_{1-x}NiMo_x$ HEAs. Firstly, all HEAs present typical brittle fractures, according to fracture morphology. The fracture surface of Fe_1Mo_0 alloy is relatively flat, with obvious river patterns, cleavage steps, and some micro-cracks (Fig. 6(a)). The cleavage steps of $Fe_{0.75}Mo_{0.25}$ alloy become more obvious. The dendrite morphology could be observed clearly besides cleavage steps in $Fe_{0.5}Mo_{0.5}$ and $Fe_{0.25}Mo_{0.75}$ alloys (Figs. 6(c) and (d)). This is consistent with dendrite morphology in BSE images (Figs. 2(d) and (e)). The cleavage steps of Fe_0Mo_1 alloy are smaller and denser due to more confusing dendritic crystals, which is confirmed in the enlarged image (Fig. 6(f)). This also shows that the second phase strengthening can improve the compression strength.

3.3 Electrochemical behavior

In order to investigate the effect of elemental Mo on the corrosion behavior of $AlCoCrFe_{1-x}NiMo_x$ alloys, the relevant tests were carried out in 3.5 wt.% NaCl solution, and potentiodynamic polarization curves are given in Fig. 7. It shows that all the HEAs exhibit passive behavior in anodic polarization. Furthermore, with the addition of Mo, the corrosion potentials shift to more negative values. The electrochemical parameters, including corrosion current density (J_{corr}), corrosion potential (φ_{corr}), pitting potential (φ_{pit}) and passive region ($\varphi_{corr}-\varphi_{pit}$), derived from Fig. 7 are listed in Table 4. The J_{corr} of Fe_1Mo_0 alloy is the lowest of all samples and its φ_{corr} is the most positive. This means that Mo-free HEA has a lower corrosion tendency and corrosion rate than Mo-containing alloys. After the addition of Mo, the corrosion galvanic cell is formed because of the generation of σ phase in the alloy, thus accelerating the corrosion rate. However, it is worth noting that the magnitude of φ_{pit} and the length of the passivation interval were larger than those of the pristine alloy when Mo content is 0.25 at.%, demonstrating that trace addition of Mo to the HEA improved the electrochemical behaviors. This is owing to the synergistic effect of Mo and Cr elements, which produces a more compact protective

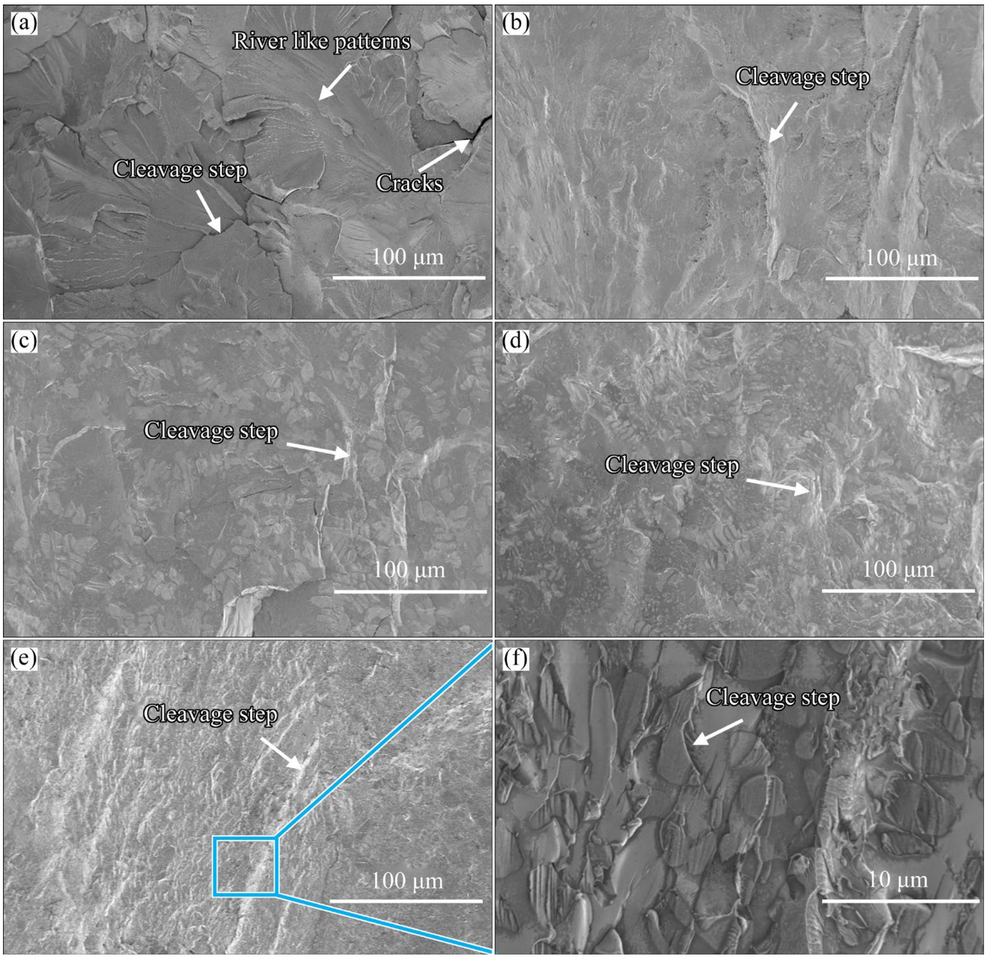

Fig. 6 Fracture surface images of $AlCoCrFe_{1-x}NiMo_x$ HEAs: (a) Fe_1Mo_0; (b) $Fe_{0.75}Mo_{0.25}$; (c) $Fe_{0.5}Mo_{0.5}$; (d) $Fe_{0.25}Mo_{0.75}$; (e, f) Fe_0Mo_1

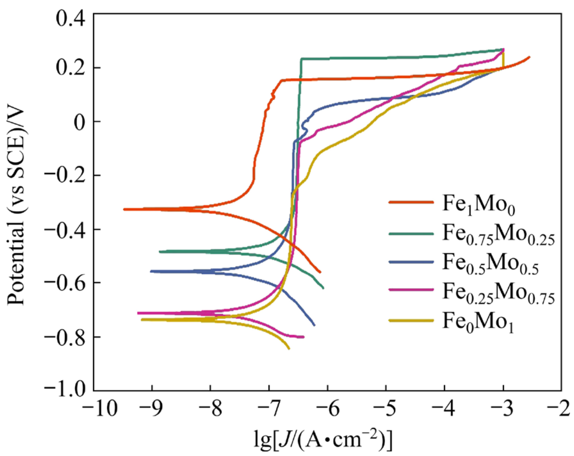

Fig. 7 Potentiodynamic polarization curves of $AlCoCrFe_{1-x}NiMo_x$ HEAs

Table 4 Electrochemical corrosion parameters of $AlCoCrFe_{1-x}NiMo_x$ HEAs derived from polarization curves (All potentials were obtained versus SCE)

Alloy	φ_{corr}/mV	φ_{pit}/mV	($\varphi_{corr}-\varphi_{pit}$)/mV	J_{corr}/(A·cm^{-2})
Fe_1Mo_0	−326	150	476	6.95×10^{-8}
$Fe_{0.75}Mo_{0.25}$	−483	231	714	8.17×10^{-8}
$Fe_{0.5}Mo_{0.5}$	−557	−77	480	9.66×10^{-8}
$Fe_{0.25}Mo_{0.75}$	−711	−79	632	1.06×10^{-7}
Fe_0Mo_1	−736	−276	460	1.12×10^{-7}

film on the alloy surface, thus enhancing corrosion resistance [42−44]. As Mo content increased from 0.5 at.% to 1.0 at.%, φ_{corr} decreased from −483 to −736 mV and φ_{pit} decreased from 231 to −276 mV. This demonstrates that the corrosion resistance of $AlCoCrFe_{1-x}NiMo_x$ HEAs is weakened on account of the adverse influence of multi-phase structures in high Mo-content HEAs.

In addition, Nyquist and Bode plots obtained from the EIS are shown in Fig. 8. As indicated in the polarization curve results, an obvious passivation occurs, confirming the presence of passive film on AlCoCrFeNiMo HAEs. According to the previous study [45], two-time constants model is commonly applied for AlCoCrFeNi HAEs which are sensitive to pitting corrosion. Meanwhile, the large phase-angle peak in the Bode diagram (Fig. 8(b)) also indicates the electrochemical system associated with two-time constants. Herein, the electric equivalent circuit consisting of two RC (resistance and capacitance) groups was utilized as displayed in Fig. 8(a), where R_1 represents the solution resistance; R_p and CPE_p correspond to the resistance and a constant-phase element related to the passive film, respectively; R_c and CPE_c are the charge-transfer resistance and double-layer capacitance, respectively. As depicted in Fig. 8, the simulated responses agree well with the experimental results, indicating that the electric equivalent circuit is suitable. The corresponding simulation parameters of electrochemical impedance spectroscopy are listed in Table 5. As indicated in Table 5, the corresponding R_p first decreases and then increases with the addition of Mo and reaches the maximum value at 0.25 at.% Mo addition, indicating a protection film under this condition. However, R_c gradually decreases with increasing the Mo content. This is because both the transformation of the phase structure and the poor protection of the passivation film formed on the multiphase structures lead to a reduction in the overall corrosion resistance of the HEAs. The higher J_{corr} of the high Mo-content HEAs in the polarization results also supports this finding.

Figure 9 shows the corrosion morphologies of Fe_1Mo_0, $Fe_{0.75}Mo_{0.25}$, and Fe_0Mo_1 alloys after the potentiometric polarization experiment. As shown in Figs. 9(a) and (b), corrosion pits with large diameters appear in Fe_1Mo_0 alloy. Table 6 gives the chemical compositions of corrosion pits and intact regions. According to the previous report [46], BCC/*B*2 matrix of the HEAs was susceptible to selective dissolution, while the grain-boundary FCC phase remained intact. Because of the large size of BCC phases in Fe_1Mo_0 alloy and similar composition between matrix and dendrite region (as shown in Fig. 2(a)), the corrosion attack by Cl^- ions occurs randomly. The inferior protection of surface film owing to large Fe amount results in large and deep pits. Therefore, the content of Al and Ni in the corrosion pits decreases to less than 5% because of their dissolution, while the content of Cr reaches more than 50%. Other than composition, the crystal structure also influences the corrosion morphology. The small grain boundary in Fe_1Mo_0 alloy with low Al content (as indicated in Table 2) is leaving from

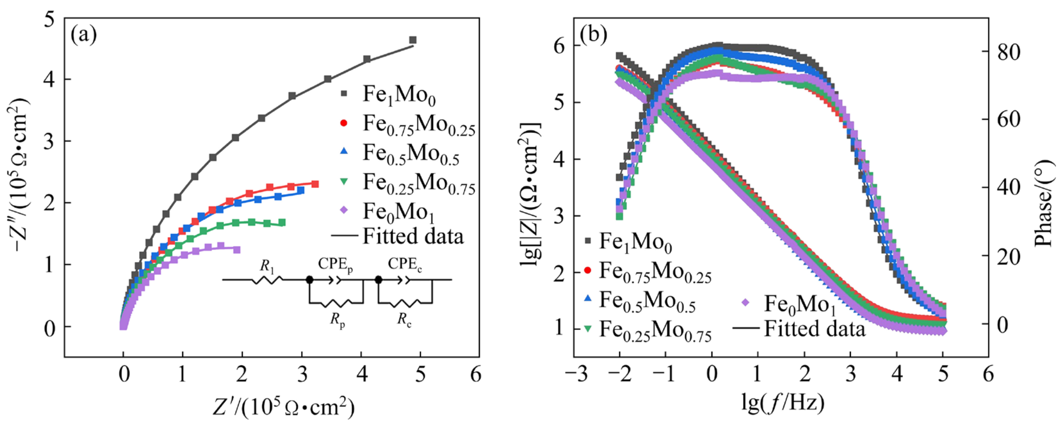

Fig. 8 EIS response of $AlCoCrFe_{1-x}NiMo_x$ HEAs at open circuit potential: (a) Nyquist plots and equivalent electrical circuit; (b) Bode plots

Table 5 Simulated parameters of $AlCoCrFe_{1-x}NiMo_x$ HEAs derived from EIS curves

Alloy	$R_1/(\Omega\cdot cm^2)$	CPE_p-T/(F·cm²)	CPE_p-P	$R_p/(\Omega\cdot cm^2)$	CPE_c-T/(F·cm²)	CPE_c-P	$R_c/(\Omega\cdot cm^2)$
Fe_1Mo_0	14.17	3.10×10^{-5}	0.87	1.13	1.24×10^{-5}	0.90	9.56×10^5
$Fe_{0.75}Mo_{0.25}$	14.32	3.23×10^{-7}	0.67	65.74	1.59×10^{-5}	0.86	5.54×10^5
$Fe_{0.5}Mo_{0.5}$	10.20	2.72×10^{-7}	0.56	57.9	1.86×10^{-5}	0.89	4.90×10^5
$Fe_{0.25}Mo_{0.75}$	12.22	1.78×10^{-8}	0.73	124.5	2.16×10^{-5}	0.87	4.07×10^5
Fe_0Mo_1	9.34	1.62×10^{-8}	0.86	224.6	2.70×10^{-5}	0.84	3.29×10^5

CPE_p-T and CPE_p-P are the capacitance value and fraction of a constant-phase element related to the passive film, respectively; CPE_c-T and CPE_c-P are the capacitance value and fraction of double-layer capacitance, respectively

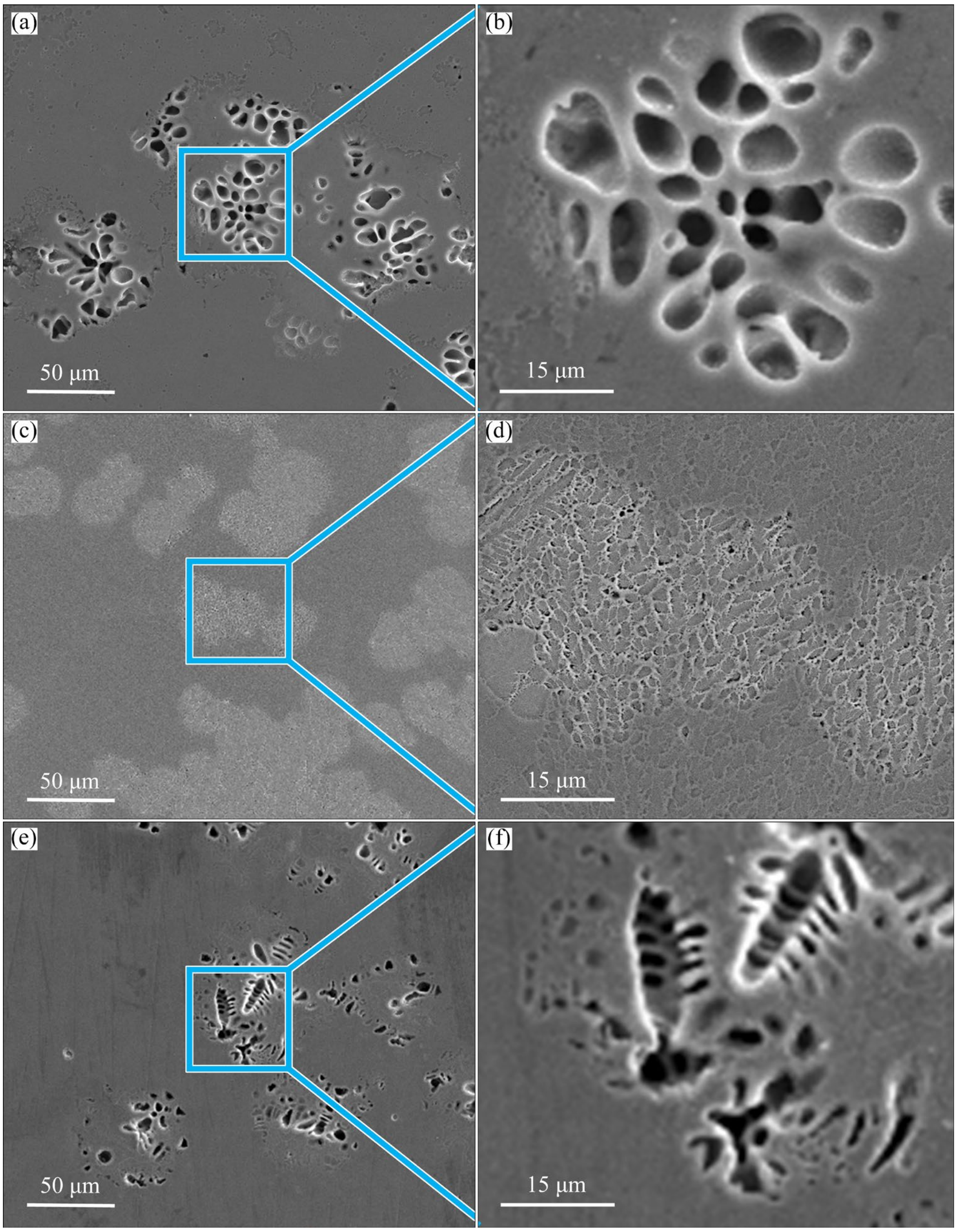

Fig. 9 Corrosion morphologies of $AlCoCrFe_{1-x}NiMo_x$ HEAs after potentiometric polarization experiments: (a, b) Fe_1Mo_0; (c, d) $Fe_{0.75}Mo_{0.25}$; (e, f) Fe_0Mo_1

corrosion attack. As a consequence, the corrosion pits are distributed randomly with big size. Figures 9(c) and (d) show the corrosion morphologies of $Fe_{0.75}Mo_{0.25}$ alloy. It is evident that the number of pits of $Fe_{0.75}Mo_{0.25}$ alloy is more than that of Fe_1Mo_0 alloy, but its diameter becomes very small, and most of the pits are distributed on the BCC phases which are rich in AlNi. The BCC phases are corroded during potentiodynamic polarization test and holes are remained. As demonstrated in Fig. 2(c), the addition of 0.25 at.% Mo leads to alternating bright and dark interconnected phases in HEAs with smaller sizes, which contributed to small corrosion pits. As indicated in Table 6, adding Mo to the $Fe_{0.75}Mo_{0.25}$ alloy results in the small size BCC phases and inter-Mo enrichment in the passive film. Cr is promoted to enrich in the oxide layer by the Mo^{6+} in the passive film, which thickens the passive film and stabilizes the Cr oxides [47]. Figures 9(e) and (f) show the corrosion morphologies of Fe_0Mo_1 alloy. The corrosion pit diameter becomes larger and the shape of the corrosion pit is similar to that of dendrite. The dendrites of Fe_0Mo_1 alloy are rich in Al and Ni elements but lack Mo

Table 6 EDS analysis results of corrosion pits and intact regions of Fe_1Mo_0, $Fe_{0.75}Mo_{0.25}$ and Fe_0Mo_1 HEAs after potentiometric polarization experiment

Alloy	Region	Content/at.%					
		Al	Cr	Fe	Co	Ni	Mo
Fe_1Mo_0	Intact	64.72	16.59	9.00	5.90	3.79	−
	Corrosion pits	0.76	53.67	25.67	16.45	3.46	−
$Fe_{0.75}Mo_{0.25}$	Intact	57.38	17.75	7.04	7.33	4.85	5.64
	Corrosion pits	0.82	47.11	19.74	19.39	4.23	8.71
Fe_0Mo_1	Intact	54.16	10.87	−	6.88	5.64	22.44
	Corrosion pits	4.51	33.23	−	24.34	10.96	26.96

and Cr elements, resulting in less Cr and Mo oxides in the formed oxide film, which seriously reduces the pitting corrosion resistance of Fe_0Mo_1 alloy. Furthermore, the corrosion is also deteriorated because of more second phases formed after 1 at.% Mo addition. Cl^- tends to accumulate at this point and attacks the passivation film continuously. After the breakdown of the passivation film, Cl^- continues to diffuse into the alloy. In the corrosion pit, the BCC phase forms a large number of galvanic cells with the σ phase, which further accelerates the corrosion rate.

4 Conclusions

(1) With the substitution of Mo element, the phases of $AlCoCrFe_{1-x}NiMo_x$ HEAs are transformed from BCC+$B2$ to BCC+σ. The addition of Mo accelerates the formation of σ phases and refines grain size of as-cast alloys.

(2) Fe_0Mo_1 HEA exhibits the best compressive fracture strength, with a fracture strain of 0. Fe_1Mo_0 alloy has the highest fracture strain of 16.82% and the lowest compressive fracture strength of 2240 MPa.

(3) The increase of the hard phase also greatly improves the hardness. The microhardness of Fe_0Mo_1 alloy is twice as high as that of Mo-free alloy.

(4) The addition of Mo elements results in a decreased corrosion resistance based on the electrochemical test results. Nevertheless, a small amount of Mo addition (x=0.25) can widen the passive region of $AlCoCrFe_{1-x}NiMo_x$ alloys.

CRediT authorship contribution statement

Hong-qi SHI: Conceptualization, Funding acquisition, Writing – Review & editing; **Xiao-di JI:** Writing – Original draft, Investigation; **Dong-hui JIAN:** Methodology, Formal analysis; **Tian-shuo XU:** Investigation; **Chen WANG:** Data curation; **Tao TANG:** Supervision; **Wen-juan LIU:** Writing – Review & editing, Supervision; **Zhen-hua CAO:** Resources.

Declaration of competing interest

The authors declare that they have no known competing financial interests or personal relationships that could have appeared to influence the work reported in this paper.

Acknowledgments

This work was supported by Suqian Sci&Tech Program Foundation, China (No. K202130), the National Natural Science Foundation of China (No. 52071176), and the Project Funded by the Priority Academic Program Development of Jiangsu Higher Education Institutions, China. The authors acknowledge Suqian Advanced Materials Industry Technology Innovation Center of Nanjing Tech University, China, for support.

References

[1] LIM K R, KWON H J, KANG J H, WON J W, NA Y S. A novel ultra-high-strength duplex Al−Co−Cr−Fe−Ni high-entropy alloy reinforced with body-centered-cubic ordered-phase particles [J]. Materials Science and Engineering A, 2020, 771: 138638.

[2] QIN Gang, CHEN Rui-run, LIAW P K, GAO Yan-fei, WANG Liang, SU Yang-qing, DING Hong-sheng, GUO Jing-jie, LI Xiao-qing. An as-cast high-entropy alloy with remarkable mechanical properties strengthened by nanometer precipitates [J]. Nanoscale, 2020, 12(6): 3965−3976.

[3] TIAN Yu-sheng, ZHOU Wen-zhe, TAN Qing-biao, WU Ming-xu, QIAO Shen, ZHU Guo-liang, DONG An-ping, SHU Da, SUN Bao-de. A review of refractory high-entropy

alloys [J]. Transactions of Nonferrous Metals Society of China, 2022, 32(11): 3487−3515.
[4] LEI Zhi-feng, LIU Xiong-jun, WU Yuan, WANG Hui, JIANG Sui-he, WANG Shu-dao, HUI Xi-dong, WU Yi-dong, GAULT B, KONTIS P, RAABE D, GU Lin, ZHANG Qing-hua, CHEN Hou-wen, WANG Hong-tao, LIU Jia-bin, AN K, ZENG Qiao-shi, NIEH Tai-gang, LU Zhao-ping. Enhanced strength and ductility in a high-entropy alloy via ordered oxygen complexes [J]. Nature, 2018, 563(7732): 546−550.
[5] WU M, BAKER I. High strength and high ductility in a novel $Fe_{40.2}Ni_{11.3}Mn_{30}Al_{7.5}Cr_{11}$ multiphase high entropy alloy [J]. Journal of Alloys and Compounds, 2020, 820: 153181.
[6] MA E, WU X L. Tailoring heterogeneities in high-entropy alloys to promote strength−ductility synergy [J]. Nature Communications, 2019, 10: 5623.
[7] GUBICZA J, HUNG P T, KAWASAKI M, HAN J K, ZHAO Y K, XUE Y F, LÁBÁR J L. Influence of severe plastic deformation on the microstructure and hardness of a CoCrFeNi high-entropy alloy: A comparison with CoCrFeNiMn [J]. Materials Characterization, 2019, 154: 304−314.
[8] WANG Hong-ming, REN Wen-xiang, LI Gui-rong, WEN Hao-ran, WANG Chang-wen, CHEN Jia-jia, ZHAO Yu-tao, CHEN Gang, KAI Xi-zhou. Microstructure and properties of $FeCoNi_{1.5}CrCu$/2024Al composites prepared by microwave sintering [J]. Materials Science and Engineering A, 2021, 801: 140406.
[9] RAZA A, ABDULAHAD S, KANG B, RYU H J, HONG S H. Corrosion resistance of weight reduced $Al_xCrFeMoV$ high entropy alloys [J]. Applied Surface Science, 2019, 485: 368−374.
[10] OSMAN H, LIU L. Additive manufacturing of high-entropy alloy composites: A review [J]. Transactions of Nonferrous Metals Society of China, 2023, 33(1): 1−24.
[11] TONG Yong-gang, CAI Yan-lin, HU Yong-le, HUANG Hong-feng, ZHANG Xian-cheng, ZHANG Hao. TiC strengthened CoCrNi medium entropy alloy: Dissolution and precipitation of TiC and its effect on microstructure and performance [J]. Transactions of Nonferrous Metals Society of China, 2022, 32(7): 2266−2275.
[12] MIRACLE D B, SENKOV O N. A critical review of high entropy alloys and related concepts [J]. Acta Materialia, 2017, 122: 448−511.
[13] ZHANG Wei-ran, LIAW P K, ZHANG Yong. Science and technology in high-entropy alloys [J]. Science China Materials, 2018, 61(1): 2−22.
[14] GEORGE E P, CURTIN W A, TASAN C C. High entropy alloys: A focused review of mechanical properties and deformation mechanisms [J]. Acta Materialia, 2020, 188: 435−474.
[15] LI Peng, SUN Hao-tian, LI Chao, WU Bao-sheng, YANG Jiang, JIANG Yu, DONG Hong-gang. A novel strengthening strategy for diffusion bonded joint of $AlCoCrFeNi_{2.1}$ eutectic high entropy alloy to 304 stainless steel [J]. Transactions of Nonferrous Metals Society of China, 2023, 33(7): 2121−2135.
[16] LIU Cong, PENG Wen-yi, JIANG Chang-shuang, GUO Hong-min, TAO Jun, DENG Xiao-hua, CHEN Zhao-xia. Composition and phase structure dependence of mechanical and magnetic properties for $AlCoCuFeNi_x$ high entropy alloys [J]. Journal of Materials Science & Technology, 2019, 35(6): 1175−1183.
[17] KARLSSON D, MARSHAL A, JOHANSSON F, SCHUISKY M, SAHLBERG M, SCHNEIDER J M, JANSSON U. Elemental segregation in an AlCoCrFeNi high-entropy alloy: A comparison between selective laser melting and induction melting [J]. Journal of Alloys and Compounds, 2019, 784: 195−203.
[18] ROGAL L, SZKLARZ Z, BOBROWSKI P, KALITA D, GARZEL G, TARASEK A, KOT M, SZLEZYNGER M. Microstructure and mechanical properties of Al−Co−Cr−Fe−Ni base high entropy alloys obtained using powder metallurgy [J]. Metals and Materials International, 2019, 25(4): 930−945.
[19] ZHOU P F, XIAO D H, YUAN T C. Microstructure, mechanical and corrosion properties of AlCoCrFeNi high-entropy alloy prepared by spark plasma sintering [J]. Acta Metallurgica Sinica (English Letters), 2020, 33(7): 937−946.
[20] ERDOGAN A, DOLEKER K M. Comparative study on dry sliding wear and oxidation performance of HVOF and laser re-melted $Al_{0.2}CrFeNi(Co,Cu)$ alloys [J]. Transactions of Nonferrous Metals Society of China, 2021, 31(8): 2428−2441.
[21] WU Chang-jun, ZHOU Chen, ZENG Jiao-feng, LIU Ya, TU Hao, SU Xu-ping. Effects of annealing at 800 and 1000 °C on phase precipitates and hardness of $Al_7Cr_{20}FeNi_{73-x}$ alloys [J]. Transactions of Nonferrous Metals Society of China, 2021, 31(7): 734−743.
[22] WANG Nai-ran, WANG Shou-ren, GOU Xiao-xiang, SHI Ze-cheng, LIN Jiang-xiang, LIU Guo-qiang, WANG Yan. Alloying behavior and characterization of $(CoCrFeNiMn)_{90}M_{10}$ (M=Al, Hf) high-entropy materials fabricated by mechanical alloying [J]. Transactions of Nonferrous Metals Society of China, 2022, 32(7): 2253−2265.
[23] FENG Jun-jie, GAO Shuo, HAN Kun, MIAO Yi-dong, QI Ji-qiu, WEI Fu-xiang, REN Yao-jian, ZHAN Zhen-zhen, SUI Yan-wei, SUN Zhi, CAO Peng. Effects of minor B addition on microstructure and properties of $Al_{19}Co_{20}Fe_{20}Ni_{41}$ eutectic high-entropy alloy [J]. Transactions of Nonferrous Metals Society of China, 2021, 31(4): 1049−1058.
[24] LI Yan-zhou, SHI Yan. Microhardness, wear resistance, and corrosion resistance of $Al_xCrFeCoNiCu$ high-entropy alloy coatings on aluminum by laser cladding [J]. Optics & Laser Technology, 2021, 134: 106632.
[25] ZHAO Yong, WANG Ming-liang, CUI Hong-zhi, ZHAO Yu-qiao, SONG Xiao-jie, ZENG Yong, GAO Xiao-hua, LU Feng, WANG Can-ming, SONG Qiang. Effects of Ti-to-Al ratios on the phases, microstructures, mechanical properties, and corrosion resistance of $Al_{2-x}CoCrFeNiTi_x$ high-entropy

alloys [J]. Journal of Alloys and Compounds, 2019, 805: 585−596.

[26] LIU Hao, SUN Shi-feng, ZHANG Tong, ZHANG Guo-zhong, YANG Hai-feng, HAO Jing-bin. Effect of Si addition on microstructure and wear behavior of AlCoCrFeNi high-entropy alloy coatings prepared by laser cladding [J]. Surface and Coatings Technology, 2021, 405: 126522.

[27] WEI R, SUN H, HAN Z H, CHEN C, WANG T, GUAN S K, LI F S. Strengthening of $Fe_{40}Mn_{40}Co_{10}Cr_{10}$ high entropy alloy via Mo/C alloying [J]. Materials Letters, 2018, 219: 85−88.

[28] CHOU Y L, YEH J W, SHIH H C. The effect of molybdenum on the corrosion behaviour of the high-entropy alloys $Co_{1.5}CrFeNi_{1.5}Ti_{0.5}Mo_x$ in aqueous environments [J]. Corrosion Science, 2010, 52(8): 2571−2581.

[29] SANTOS R F, ROCHA A M, BASTOS A C, CARDOSO J P, RODRIGUES F, FERNANDES C M, SACRAMENTO J, FERREIRA M G S, SENOS A M R, FONSECA C. Microstructural characterization and corrosion resistance of WC−Ni−Cr−Mo composite — The effect of Mo [J]. International Journal of Refractory Metals and Hard Materials, 2020, 86: 105090.

[30] WANG W R, WANG Wei-lin, WANG S C, TSAI Y C, LAI Chun-hui, YEH J W. Effects of Al addition on the microstructure and mechanical property of $Al_xCoCrFeNi$ high-entropy alloys [J]. Intermetallics, 2012, 26: 44−51.

[31] HSU C Y, SHEU T S, YEH J W, CHEN S K. Effect of iron content on wear behavior of $AlCoCrFe_xMo_{0.5}Ni$ high-entropy alloys [J]. Wear, 2010, 268(5/6): 653−659.

[32] JIN Xi, LIANG Yu-xin, BI Juan, LI Bang-sheng. Non-monotonic variation of structural and tensile properties with Cr content in $AlCoCr_xFeNi_2$ high entropy alloys [J]. Journal of Alloys and Compounds, 2019, 798: 243−248.

[33] JIN Ze-yu, LV Juan, JIA Heng-lei, LIU Wei-hong, LI Huang-long, CHEN Zu-huang, LIN Xi, XIE Guo-qiang, LIU Xing-jun, SUN Shu-hui. Nanoporous Al−Ni−Co−Ir−Mo high-entropy alloy for record-high water splitting activity in acidic environments [J]. Small, 2019, 15(47): 1904180.

[34] ZHU Chen-long, LI Zhan-jiang, HONG Chun-fu, DAI Pin-qiang, CHEN Jun-feng. Microstructure and mechanical properties of the TiZrNbMoTa refractory high-entropy alloy produced by mechanical alloying and spark plasma sintering [J]. International Journal of Refractory Metals and Hard Materials, 2020, 93: 105357.

[35] ZHANG Hui-bin, GUO Fei, WAN Lei-lei, GAO Zheng-cheng, CHEN Tao-tao, CAO Hua-zhen, CHEN Hong-yu, ZHENG Guo-qu. Performance assessments of porous $FeCoNiCrAl_x$ high-entropy alloys in high-temperature oxidation, carbonization and sulfidation atmospheres [J]. Journal of Alloys and Compounds, 2023, 930: 167437.

[36] LU Yi-ping, GAO Xu-zhou, JIANG Li, CHEN Zong-ning, WANG Tong-min, JIE Jin-chuan, KANG Hui-jun, ZHANG Yu-bo, GUO Sheng, RUAN Hai-hui. Directly cast bulk eutectic and near-eutectic high entropy alloys with balanced strength and ductility in a wide temperature range [J]. Acta Materialia, 2017, 124: 143−150.

[37] ZHU J M, ZHANG H F, FU H M, WANG A M, LI H, HU Z Q. Microstructures and compressive properties of multicomponent $AlCoCrCuFeNiMo_x$ alloys [J]. Journal of Alloys and Compounds, 2010, 497: 52−56.

[38] XIAO D H, ZHOU P F, WU W Q, DIAO H Y, GAO M C, SONG M, LIAW P K. Microstructure, mechanical and corrosion behaviors of AlCoCuFeNi-(Cr,Ti) high entropy alloys [J]. Materials & Design, 2017, 116: 438−447.

[39] ZHOU Y J, ZHANG Y, WANG Y L, CHEN G L. Solid solution alloys of $AlCoCrFeNiTi_x$ with excellent room-temperature mechanical properties [J]. Applied Physics Letters, 2007, 90(18): 181904.

[40] KANG M J, LIM K R, WON J W, NA Y S. Effect of Co content on the mechanical properties of *A*2 and *B*2 phases in $AlCo_xCrFeNi$ high-entropy alloys [J]. Journal of Alloys and Compounds, 2018, 769: 808−812.

[41] ZHU J M, FU H M, ZHANG H F, WANG A M, LI H, HU Z Q. Microstructure and compressive properties of multiprincipal component $AlCoCrFeNiC_x$ alloys [J]. Journal of Alloys and Compounds, 2011, 509(8): 3476−3480.

[42] EBRAHIMI N, JAKUPI P, NOEL J J, SHOESMITH D W. The role of alloying elements on the crevice corrosion behavior of Ni−Cr−Mo alloys [J]. Corrosion, 2015, 71(12): 1441−1451.

[43] QUIAMBAO K F, MCDONNELL S J, SCHREIBER D K, GERARD A Y, FREEDY K M, LU P, SAAL J E, FRANKEL G S, SCULLY J R. Passivation of a corrosion resistant high entropy alloy in non-oxidizing sulfate solutions [J]. Acta Materialia, 2019, 164: 362−376.

[44] LI X J, HENDERSON J D, FILICE F P, ZAGIDULIN D, BIESINGER M C, SUN F, QIAO B N, SHOESMITH D W, NOEL J J, OGLE K. The contribution of Cr and Mo to the passivation of $Ni_{22}Cr$ and $Ni_{22}Cr_{10}Mo$ alloys in sulfuric acid [J]. Corrosion Science, 2020, 176: 109015.

[45] PARAKH A, VAIDYA M, KUMAR N, CHETTY R, MURTY B S. Effect of crystal structure and grain size on corrosion properties of AlCoCrFeNi high entropy alloy [J]. Journal of Alloys and Compounds, 2021, 863: 158056.

[46] YAMANAKA K, SHIRATORI H, MORI M, OMURA K, FUJIEDA T, KUWABARA K, CHIBA A, Corrosion mechanism of an equimolar AlCoCrFeNi high-entropy alloy additively manufactured by electron beam melting [J]. NPJ Materials Degradation, 2020, 4: 24.

[47] SONG Dan, HAO Jun, YANG Fa-lin, CHEN Huan-de, LIANG Ning-ning, WU Yuan-yuan, ZHANG Jian-chun, MA Han, KLU E E, GAO Bo, QIAO Yan-xin, SUN Jia-peng, JIANG Jin-yang. Corrosion behavior and mechanism of Cr−Mo alloyed steel: Role of ferrite/bainite duplex microstructure [J]. Journal of Alloys and Compounds, 2019, 809: 151787.

Mo 取代 Fe 对 $AlCoCrFe_{1-x}NiMo_x$ 高熵合金强度和耐蚀性能的影响

师红旗[1]，季晓迪[2]，简东慧[2]，徐天烁[1]，王 宸[2]，汤 涛[2,3]，刘文娟[2,3]，操振华[2,3]

1. 宿迁学院 信息工程学院，宿迁 223800；
2. 南京工业大学 材料科学与工程学院，南京 211816；
3. 南京工业大学 江苏先进无机功能复合材料协同创新中心，南京 211816

摘　要：制备一系列 $AlCoCrFe_{1-x}NiMo_x$ 高熵合金，并通过 XRD、SEM、EDS、压缩试验、硬度和电化学测试对其进行表征。研究结果表明，Mo 完全取代 Fe 后，合金抗压强度可达 3181 MPa，这是因为 Mo 的加入可以形成有利于晶粒细化的 σ 相，从而提高合金强度。然而，由于 Mo 添加后基体和 σ 相之间形成腐蚀原电池，Mo 添加对其耐腐蚀性能具有不利影响。虽然大部分 $AlCoCrFe_{1-x}NiMo_x$ 合金比原始合金的腐蚀电流密度低，但 Mo 取代量 x=0.25 时，拓宽了高熵合金的钝化区间。$AlCoCrFe_{1-x}NiMo_x$ 高熵合金力学性能与耐蚀性能的不一致可归因于 Mo 的添加对相形成和钝化膜保护的不同作用。

关键词：高熵合金；Mo 取代 Fe；抗压强度；耐蚀性能

(Edited by Wei-ping CHEN)